On the Use of Spatial and Spectral Redundancy to Speed-Up Brillouin Micro-Imaging

Brechet Leo, Gilet Valentin, Loumaigne Matthieu, Nizar Bouhlel, Guillaume Mabilleau, Rousseau David

On the use of spatial and spectral redundancy to speed-up Brillouin micro-imaging

1st Brechet Leo
LARIS, UMR IRHS INRAe
Université d'Angers
Angers, France
leo.brechet@univ-angers.fr

2nd Gilet Valentin
LARIS, UMR IRHS INRAe
Université d'Angers
Angers, France
valentin.gilet@univ-angers.fr

3rd Loumaigne Matthieu
MOLTECH-Anjou, UMR CNRS 6200,
Université d'Angers
Angers, France
matthieu.loumaigne@univ-angers.fr

4th Bouhlel Nizar
INRAE, IRHS, SFR QuaSaV
Institut Agro, Université d'Angers
Angers, France
nizar.bouhlel@agrocampus-ouest.fr

5th Mabilleau Guillaume
RMeS, REGOS, SFR ICAT
CHU Angers, Université d'Angers
Angers, France
guillaume.mabilleau@univ-angers.fr

6th Rousseau David
LARIS, UMR IRHS INRAe
Université d'Angers
Angers, France
david.rousseau@univ-angers.fr

***Abstract*—We propose a smart scanning protocol to speed up the acquisition of Brillouin microscopy. It is based on a two-pass algorithm. In a first pass at low signal-to-noise-ratio (SNR), essential pixels located on the convex hull of the Fourier phasor space of the sample are identified, selected and rescanned at high SNR. These essential spectra serve as a decomposition basis for the remaining spectra located inside the convex hull. A second acceleration is gained through the use of superpixels computed on a denoised version of the low SNR image. It allows to reduce the number of pixels on which Brillouin spectra are to be estimated. This protocol recently introduced for Raman microscopy is tested here for the first time on Brillouin hyperspectral images (HSI). A compression by a factor between 3 and 253 with very limited distortion is demonstrated on simulated samples fitted on real samples of cell bones. Further opportunities of improvement are identified and discussed.**

***Index Terms*—Brillouin, micro-imaging, smart scanning, phasor, superpixels**

I. Introduction

Brillouin microscopy [1] represents a valuable imaging technique for mapping and mechanically characterizing cellular structures. A current limitation of the technique is the acquisition time which is not systematically compatible with real-time imaging of in vivo samples. This is intrinsically linked with the point-by-point raster-scanning of the sample. The resulting acquisition times can range from a few to tens of minutes for extended samples. Consequently, an open research front of science is to accelerate the data acquisition in Brillouin micro-imaging via computational approaches [2]. These approaches differ by their method and by the informational tasks that they address.

Some accelerations can be achieved via the instrumentation itself, e.g., involving line scanning [3], [4] or reducing the laser exposure time [5]. Apart from these physical approach few has been done on the side of the spectral and spatial signal analysis [6], [7] for these images while the hyperspectral Brillouin data are obviously very redundant both in the spectral and spatial domain. Recently, an approach combining spatial domain compression and spectral domain compression [8] has allowed for a 1000-fold reduction in acquisition time in Raman micro-imaging. In [8], authors mentioned that their acquisition protocol can be extended to other hyperspectral microscopy.

In [8] and the related articles [9]–[11] authors assume that the spectral information of the sample can be recovered from only few pixels, called essential spectra, of the hyperspectral image. These essential spectra form a convex hull of the data points in a reduced space. This brings a first source of acceleration in the acquisition. Another source of acceleration comes with the use of superpixels to encode the acquired image. In this communication, we investigate the value of the protocol introduced in [8] for Brillouin microscopy.

II. Material and methods

A. Methods

Figure 1 represents the smart scanning protocol described in [8] which is revisited here for Brillouin microscopy. Briefly, this scanning protocol consists in a first fast acquisition, i.e. at low SNR, of the whole sample to produce $\mathrm{I}_{\mathrm{low}}(x, y, \lambda)$, an HSI made of $X \times Y$ pixels and L wavelengths. Then, a dimension reduction is applied along λ to obtain $\mathrm{I}_{\mathrm{mono}}$, a mono component image, which is then segmented into P superpixels using SLIC [12] to produce $\mathrm{I}_{\mathrm{seg}}$. A subset of the spectra can be extracted from $\mathrm{I}_{\mathrm{low}}$ by selecting the centroids of the superpixels (x_p, y_p), with p ranging from 1 to P. It represents the compression in the spatial domain.

As a parallel branch of the pipeline, a discrete Fourier transform is computed on $\mathrm{I}_{\mathrm{low}}$ along the wavelength domain. It results in the the decomposition of each spectra constituting

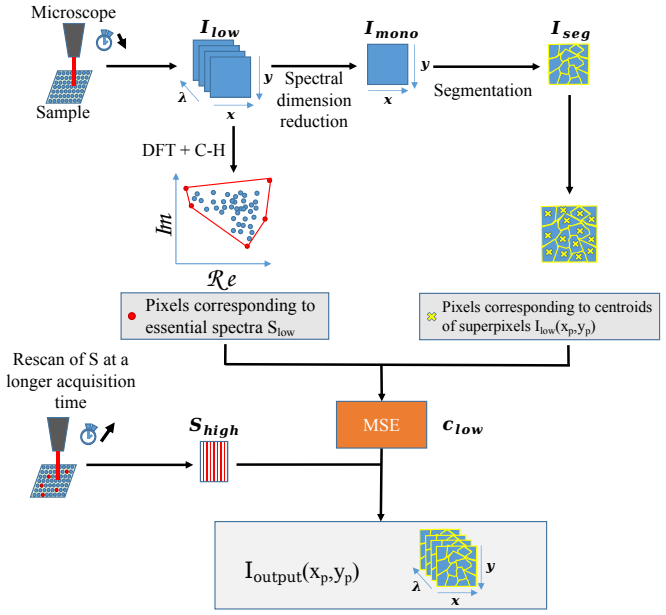

Fig. 1. Pipeline of the protocol proposed in [8].

the HSI in elementary waves

$$I_{\text{low}}(x,y)_l = \frac{1}{L}\sum_{r=1}^{L}(G_r(x,y)+jQ_r(x,y)) \exp\left(j\frac{2\pi}{L}(l-1)(r-1)\right), \tag{1}$$

with the real numbers $G_r(x,y)$ and $Q_r(x,y)$ which can be seen as coordinates of the r-th phasor involved in the Fourier representation, and j the imaginary number. For a defined value of r, we compute the convex hull of the points cloud represented by $G_r(x,y)$ and $Q_r(x,y)$. The pixels corresponding to the phasors located on this convex hull are associated to the most linearly dissimilar spectra, the so-called essential spectra. They constitute another subset of spectra that we gather in S_{low} a matrix containing K essential spectra along rows and L spectral bands along columns. It represents the compression in the spectral domain.

Therefrom, a mean square error (MSE) is used to unmix the spectra of $\text{I}_{\text{low}}(x_p,y_p)$ with respect to the spectra of S_{low}. It leads to a matrix of concentration $\boldsymbol{c}_{\text{low}}$ containing the K concentrations associated with the essential spectra for the pixel located at (x_p,y_p) along the rows for the P centroids along the columns. It can be formally expressed as

$$\text{I}_{\text{low}}(x_p,y_p) = \text{S}_{\text{low}}^T \boldsymbol{c}_{\text{low}}(x_p,y_p), \tag{2}$$

with $\boldsymbol{c}_{\text{low}}(x_p,y_p)$, the estimated mixture proportion.

Rescanning only the essential spectra during a longer exposure, i.e. higher signal, produces S_{high} which allows to reconstruct each centroid of superpixel with a higher signal

$$\text{I}_{\text{output}}(x_p,y_p) = \text{S}_{\text{high}}^T \boldsymbol{c}_{\text{low}}(x_p,y_p)\ . \tag{3}$$

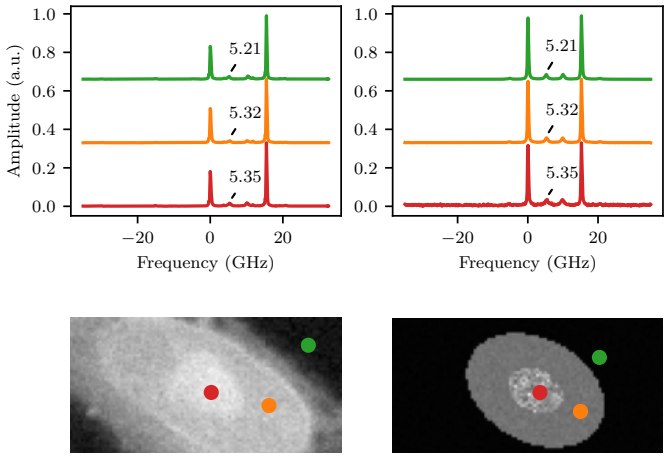

Fig. 2. Comparison between real data (on the left) and simulated data (on the right). The first row shows the spectra corresponding to the pixels pointed with matching color cross on the images of the second row. The real and simulated data SNR are estimated to 17 dB. The value indicated corresponds to the spectral value in GHz of the Brillouin shift.

The produced output image is made of superpixels with homogeneous spectra as given in (3).

B. Dataset

The protocol described in II-A has been tested on simulated Brillouin microscopy data and we now detail the simulator created to generate realistic synthetic data. Similarly to [8] we started with an initialization of an empty image of size $X \times Y$ where we randomly put some object corresponding to materials with homogeneous Brillouin parameters. In this communication, to mimic cells, as shown in Fig. 2, we generated ellipses representing (a) the nucleus which includes (b) the cytoplasm and we filled the remaining room with pixels corresponding to (c) water.

The spectrum of each of these materials is made of Rayleigh rays and Brillouin rays which are classically modelled respectively as an Asymmetric Pseudo-Voigt [13]

$$R(\nu,\nu_R,H_R,\alpha_1,\alpha_2,w_R) = H_R \times \begin{cases} \alpha_1 \left[\frac{1}{1+\left(\frac{\nu-\nu_R}{w_R/2}\right)^2}\right] \\ +(1-\alpha_1)\, e^{\left[-\ln 2\left(\frac{\nu-\nu_R}{w_R/2}\right)^2\right]} \end{cases} ; \nu < \nu_R$$
$$H_R \times \begin{cases} \alpha_2 \left[\frac{1}{1+\left(\frac{\nu-\nu_R}{w_R/2}\right)^2}\right] \\ +(1-\alpha_2)\, e^{\left[-\ln 2\left(\frac{\nu-\nu_R}{w_R/2}\right)^2\right]} \end{cases} ; \nu \geq \nu_R \tag{4}$$

and a Lorentzian

$$B(\nu,\nu_B,H_B,w_B) = H_B \frac{1}{1+\left(\frac{\nu-\nu_B}{w_B/2}\right)^2} \tag{5}$$

functions with ν the frequency and ν_R, ν_B, H_R, H_B, α_1, α_2, w_R, w_B the parameters described in Fig. 3.

These spectral information are further corrupted with a classical thermal noise (i.e. an iid Gaussian noise) which can be modeled as an independent and identically distributed Gaussian noise. The simulator of Brillouin microscopy data described aboved was tuned to fit with data from real sample. We used as real sample cells of bones imaged with a $\times 60$ objective. To excite the sample, a 785 nm Rubidium laser was used. The diffuse light emitted by the sample was then split with a virtually imaged phased array (VIPA) device and collected by a complementary metal-oxide-semiconductor (CMOS) sensor. Several replicated measurements at different acquisition times were performed to study the relation between the signal-to-noise ratio

$$\text{SNR} = 10 \log_{10} \left(\frac{I}{\sigma_N} \right), \tag{6}$$

that we defined as the ratio of the maximum intensity of the Brillouin peak I and the standard deviation of the thermal noise σ_N, and the acquisition time. These multiple acquisitions allowed us to estimate t_{base}, the minimum time taken by the equipment between two acquisitions. The similarity of the real and generated data are shown in Fig. 2 both in the spectral and spatial domain. One can recognize the Rayleigh peaks at 0 and 15 GHz, the Brillouin anti-Stokes peaks at 5 and 20 GHz and the Brillouin Stokes peaks at -5 and 10 GHz. Multiple Rayleigh and Brillouin peaks appear on the spectrum due to different order of diffraction of the light. The Brillouin peak of interest for the extraction of mechanical properties (see (6)) is the anti-Stokes of the first order, spotted here around 5 GHz. The magnitude of the Brillouin shift for each component of the cells is provided in Fig. 2. On the real spectra one the Rayleigh peaks do not have the same amplitude. This is due to the position of the frequency of the laser cavity which may

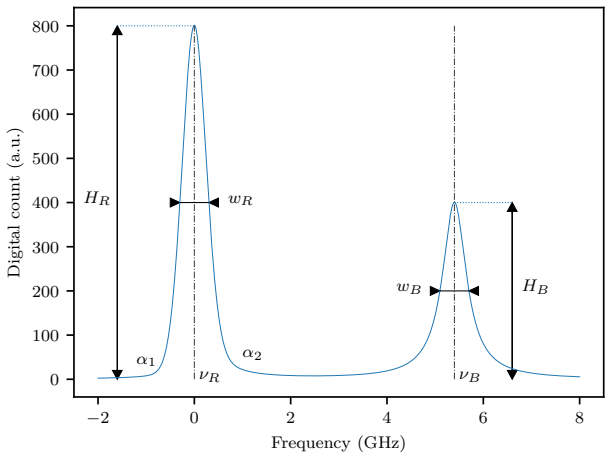

Fig. 3. Description of parameters of the simulated spectrum where R stands for Rayleigh and B Brillouin. H_R and H_B correspond to the amplitudes, w_R and w_B the full width half maximum (FWHM), ν_R and ν_B the position of the maximum, and α_1 and α_2 parameters that give asymmetry.

TABLE I
ESTIMATED VALUES OF THE LORENTZIAN CURVE, CORRESPONDING TO THE BRILLOUIN PEAK ON THE REAL DATA. ν_B AND w_B ARE IN GHZ, H_B IN ARBITRARY UNIT.

	H_B	ν_B	w_B
Nucleus (a)	62.89	5.35	0.86
Cytoplasm (b)	291.27	5.32	0.85
Matrix, i.e. water (c)	1390.78	5.21	0.79

not be centered on the part of interest of the spectra. As visible in Fig. 2, we choose not to include this aspect in our model.

The detail of parameters H_B, ν_B and w_B which have been used to build the synthetic data through (4) and (5) are provided in Table I. The built in synthetic dataset has been composed of 90 HSI of the same simulated sample at different SNR, ranging from 5 dB to 24 dB in order to assess the robustness and the gain in time of the protocol. To provide an estimation of the noise-induced variance, we replicated the same HSI five times for each SNR. The HSI corresponding to the SNR of 24 dB will be taken as a reference for assessment, we designated it as $\boldsymbol{I}_{\text{ref}}$. $\boldsymbol{I}_{\text{ref}}$ will also be used to simulate the second pass at a higher SNR, we will thus collect $\boldsymbol{S}_{\text{high}}$ in it.

C. Metrics

To evaluate the reconstruction of the HSI by the protocol described in II-A, we decided to focus on the assessment of the restitution of the anti-Stokes Brillouin peak of the first order across the entire HSI. Its characterization is indeed essential to study the composition of the sample since it carries most of its mechanical properties. Thus, for each pixel of the reconstructed HSI, we computed the mean absolute error (MAE) of the shift

$$\nu_{\text{err}} = \frac{1}{XY} \sum_{x=1}^{X} \sum_{y=1}^{Y} |\nu_B(x,y) - \nu_{\text{ref}}(x,y)|, \tag{7}$$

and of the FWHM

$$w_{\text{err}} = \frac{1}{XY} \sum_{x=1}^{X} \sum_{y=1}^{Y} |w_B(x,y) - w_{\text{ref}}(x,y)|, \tag{8}$$

with $\nu_B(x,y)$ and $w_B(x,y)$ the Brillouin shift and FWHM estimated on $\boldsymbol{I}_{\text{output}}(x,y)$, and $\nu_{\text{ref}}(x,y)$ and $w_{\text{ref}}(x,y)$ estimated on $\boldsymbol{I}_{\text{ref}}(x,y)$ by fitting (5) on the reconstructed data using least mean square method. The fit also allows to estimate the amplitudes H_B and $H_{\text{ref}}(x,y)$, giving us the possibility to calculate

$$\phi = \frac{1}{XY} \sum_{x=1}^{X} \sum_{y=1}^{Y} \frac{H_B(x,y) w_B(x,y)}{H_{\text{ref}}(x,y) w_{\text{ref}}(x,y)}, \tag{9}$$

the ratio between the area under the curve of $\boldsymbol{I}_{\text{output}}(x,y)$ and $\boldsymbol{I}_{\text{ref}}(x,y)$. MAE has been chosen to penalize outliers. Furthermore, we evaluated the processing time of the entire acquisition process, encompassing the time required for acquiring $\boldsymbol{I}_{\text{low}}$, computing the protocol and the rescan of the essential spectra $\boldsymbol{S}_{\text{high}}$.

III. Results

The assessment of the scanning protocol for various SNR is in Fig. (4). Error on the Brillouin shift ν_{err}, the FWHM w_{err} and the Integral ratio ϕ are trivially degraded as the SNR decreases but with a relative plateau located at 17 dB which appears as a possible tradeoff between compression and distorsion. The recorded error amplitudes appear small in absolute amplitude. However, one has to relate these amplitudes with the expected difference between each material composing the sample itself. Table I indicates a minimum difference of 0.04 between the standard ν_B values of the different material composing our sample. Interestingly, even at the lowest tested SNR ν_{err} reaches only 0.014. This means that even at these low SNR a distinction between the materials should be possible.

Table II exhibits the protocol time for three SNR values chosen as follow: 5.4, the minimum value; 17, the location of the plateau; 21, the maximum value. The reference is also given for comparison. The first pass of the acquisition appears to be the bottleneck of the protocol, representing at least 95% of the total time. Nevertheless, a 3 fold compression factor in time and limited distorsion seems to be possible via a first pass around 17 dB, with our protocol.

As a complement to the quantitative assessment of our method, we propose in Fig. 5 a qualitative visual appreciation of the results provided both in the spatial domain after superpixelisation and after estimation of the Brillouin spectra. The estimated spectra show a good quality on the Brillouin part even at low SNR thanks to the use of essential spectra. However, it is to be noticed that the distortion on the spectra differ from one material to another. The most represented material (water here in orange in Fig. 5) has a perfect estimation independently of the SNR while the noise has much more impact on the areas of the samples with fewer pixels. This may be due to the fact that the protocol introduced has been used on the full spectra as in [8]. This is of course fully relevant for Raman microscopy but can be criticized for Brillouin microscopy where the mechanical information lay on the Brillouin part. Changing the seek of essential spectra by first masking the Rayleigh peaks should probably enhance the distinction between the materials and allow to select better representatives for the essential spectra. Dimension reduction step leading to I_{mono} would also benefit from this modification and allow a segmentation more specifically oriented toward the Brillouin information.

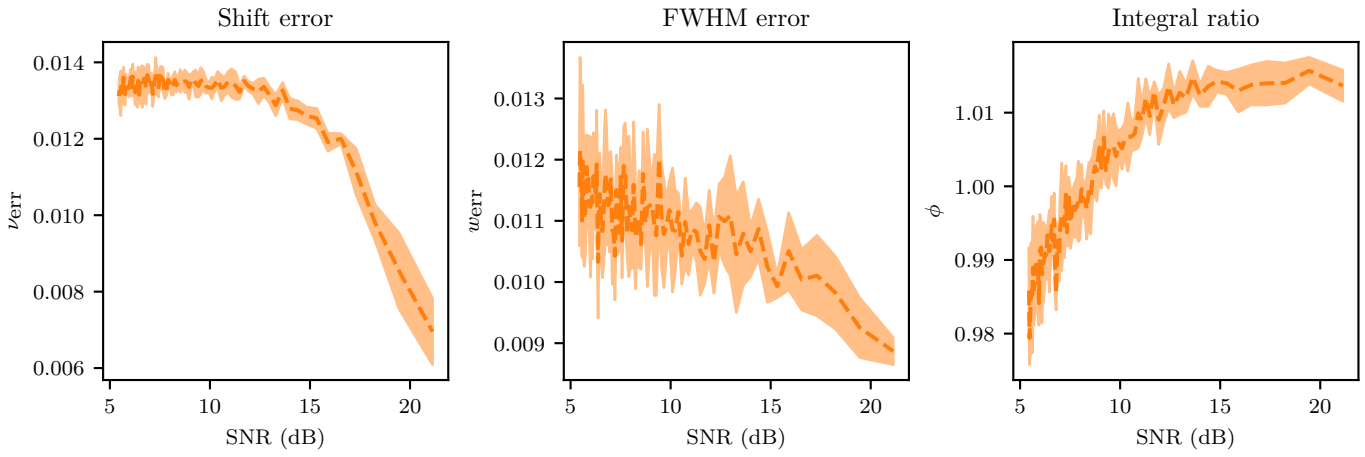

Fig. 4. Metrics of performance, respectively from left to right spectral shift, FWHM and integral ratio for the estimated Brillouin parameters defined in (7), (8) and (9) as a function of SNR. Average value in dot line, standard deviation in bold. Results presented here are obtained for $100 \times 100 \times 940$ HSI with the following parameters: number of harmonics r=3, number of superpixels P=1000 and a SLIC compactness of 0.1.

TABLE II
DETAILED TIME TAKEN BY THE PROPOSED SCANNING PROTOCOL ASSOCIATED WITH THE PERFORMANCE METRICS SPECTRAL SHIFT, FWHM AND INTEGRAL RATIO FOR THE ESTIMATED BRILLOUIN PARAMETERS DEFINED IN (7), (8) AND (9) FOR THREE VALUES OF SNR.

First pass SNR	Protocol time (s)				Metrics		
	First pass	Processing time	Second pass	Total	ν_{err}	w_{err}	ϕ
5.45	336.5	4.8	11.6	352.9	0.013	0.012	0.986
17.32	861.4	4.7	11.6	877.7	0.011	0.010	1.014
21.13	1649.8	4.8	12.5	1667.1	0.007	0.009	1.01
Reference	3037.1			3037.1	0	0	1

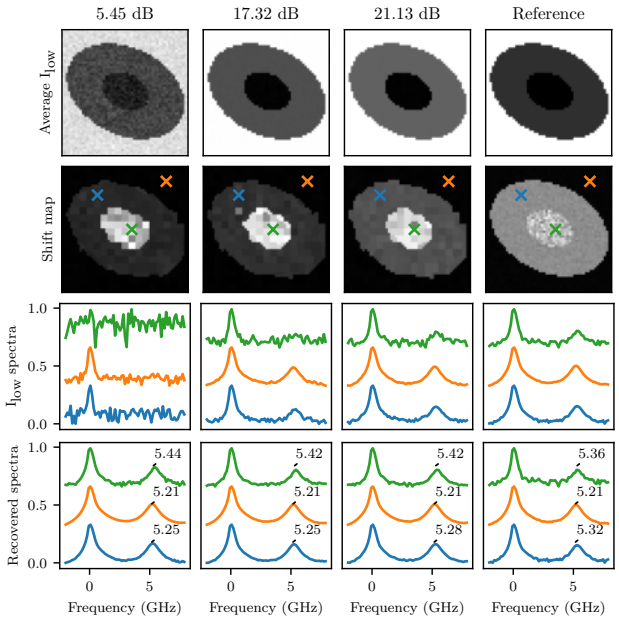

Fig. 5. Qualitative assessment of the protocol for the three SNR presented in Tab. II. First row is for the image resulting from the averaging of the I_{low} spectra. Second row gives the recovered Brillouin shift map obtained with the protocol. Third row gives the low SNR spectra acquired on the position indicated in the images of the second row. Fourth row gives the I_{output} spectra, where the value of the recovered Brillouin shift is indicated. Spectral and spatial domain are here cropped to the part of interest and presented in log scale to allow a better visualization (see Fig. 2).

IV. Conclusion

In this communication, we extended the protocol recently proposed in [8] to Brillouin microscopy data. A 3 fold compression factor in time seems to be possible with a limited distortion of the spectra. It is far from the $1000\times$ compression mentioned in [8]. This can be easily understood since the acquisition time in Raman microscopy is much larger than in Brillouin microscopy.

A higher compression of $253\times$ could even be reached if, as also proposed in [8], the first pass could be replaced by another full-frame fast imaging modality which could help in the superpixelization of the image. This indeed is accessible in practice. For instance, fluorescence imaging, or differencial interference contrast (DIC) (to remain dye-free), could be used as candidate for this full-frame fast image replacing the first raster scan. These are interesting perspectives that we currently investigate to optimize the use of spatial and spectral redundancy in Brillouin data via smart computational micro-imaging.

Acknowledgment

This project has received funding from the European Innovation Council through its Horizon Europe Pathfinder Programme under grant agreement No 101098989. Funded by the European Union. Authors thank Giancarlo Ruocco, Claudia Testi and Li Zhang Center for Life NanoScience, Istituto Italiano di Tecnologia for acquisition of the real sample used for illustration in this communication. Valentin Gilet gratefully acknowledge financial support from the "ANR-21-CE29-0007" project (Agence Nationale de la Recherche).

References

[1] I. Kabakova, J. Zhang, Y. Xiang, S. Caponi, A. Bilenca, J. Guck, and G. Scarcelli, "Brillouin microscopy," *Nature Reviews Methods Primers*, vol. 4, no. 1, p. 8, 2024.

[2] G. Antonacci, T. Beck, A. Bilenca, J. Czarske, K. Elsayad, J. Guck, K. Kim, B. Krug, F. Palombo, R. Prevedel *et al.*, "Recent progress and current opinions in brillouin microscopy for life science applications," *Biophysical Reviews*, vol. 12, pp. 615–624, 2020.

[3] J. Zhang, A. Fiore, S.-H. Yun, H. Kim, and G. Scarcelli, "Line-scanning brillouin microscopy for rapid non-invasive mechanical imaging," *Scientific reports*, vol. 6, no. 1, p. 35398, 2016.

[4] N. Khalilgharibi, G. Paci, and Y. Mao, "Line-scanning speeds up brillouin microscopy," *Nature Methods*, vol. 20, no. 5, pp. 643–644, 2023.

[5] F. Yang, C. Bevilacqua, S. Hambura, A. Neves, A. Gopalan, K. Watanabe, M. Govendir, M. Bernabeu, J. Ellenberg, A. Diz-Muñoz *et al.*, "Pulsed stimulated brillouin microscopy enables high-sensitivity mechanical imaging of live and fragile biological specimens," *Nature Methods*, vol. 20, no. 12, pp. 1971–1979, 2023.

[6] Y. Xiang, K. L. C. Seow, C. Paterson, and P. Török, "Multivariate analysis of brillouin imaging data by supervised and unsupervised learning," *Journal of Biophotonics*, vol. 14, no. 7, p. e202000508, 2021.

[7] M. Alunni Cardinali, M. Govoni, M. Tschon, S. Brogini, L. Vivarelli, A. Morresi, D. Fioretto, M. Rocchi, C. Stagni, M. Fini *et al.*, "Brillouin–raman micro-spectroscopy and machine learning techniques to classify osteoarthritic lesions in the human articular cartilage," *Scientific Reports*, vol. 13, no. 1, p. 1690, 2023.

[8] V. Gilet, G. Mabilleau, M. Loumaigne, L. Coic, R. Vitale, T. Oberlin, J. H. de Morais Goulart, N. Dobigeon, C. Ruckebusch, and D. Rousseau, "Superpixels meet essential spectra for fast raman hyperspectral microimaging," *Optics Express*, vol. 32, no. 1, pp. 932–948, 2024.

[9] L. Coic, P.-Y. Sacré, A. Dispas, C. De Bleye, M. Fillet, C. Ruckebusch, P. Hubert, and E. Ziemons, "Pixel-based raman hyperspectral identification of complex pharmaceutical formulations," *Analytica Chimica Acta*, vol. 1155, p. 338361, 2021.

[10] L. Coic, P.-Y. Sacre, A. Dispas, C. De Bleye, M. Fillet, C. Ruckebusch, P. Hubert, and E. Ziemons, "Selection of essential spectra to improve the multivariate curve resolution of minor compounds in complex pharmaceutical formulations," *Analytica Chimica Acta*, vol. 1198, p. 339532, 2022.

[11] L. Coic, R. Vitale, M. Moreau, D. Rousseau, J. H. de Morais Goulart, N. Dobigeon, and C. Ruckebusch, "Assessment of essential information in the fourier domain to accelerate raman hyperspectral microimaging," *Analytical Chemistry*, vol. 95, no. 42, pp. 15 497–15 504, 2023.

[12] R. Achanta, A. Shaji, K. Smith, A. Lucchi, P. Fua, and S. Süsstrunk, "Slic superpixels compared to state-of-the-art superpixel methods," *IEEE Transactions on Pattern Analysis and Machine Intelligence*, vol. 34, no. 11, pp. 2274–2282, 2012.

[13] C. D. Wijetunge, I. Saeed, B. A. Boughton, U. Roessner, and S. K. Halgamuge, "A new peak detection algorithm for maldi mass spectrometry data based on a modified asymmetric pseudo-voigt model," *BMC genomics*, vol. 16, pp. 1–12, 2015.